Design, computational and experimental investigation of a small-scale turbopump for organic Rankine cycle systems

Sajjad Zakeralhoseini [*], Jürg Schiffmann

Ecole Polytechnique Fédérale de Lausanne (EPFL), Laboratory for Applied Mechanical Design, CH-1015 Lausanne, Switzerland

ABSTRACT

The hydraulic design, computational analysis, and experimental investigations of a high-speed small-scale turbopump for mobile waste heat recovery applications based on organic Rankine cycle systems are presented in this paper. Such applications demand high-pressure rise, lightweight, and compact pumping systems with simple construction. The investigated turbopump features an unshrouded 37.75 mm tip diameter single-stage centrifugal pump equipped with eight radial blades, eight splitters blades, and a rectangular axisymmetric volute. The pump should deliver 0.28 kg/s of mass flow rate with a pressure rise of 20 bar at a designed rotational speed of 25,000 rpm. Due to uncertainties observed in employing state-of-the-art 1-d methods that are valid for much larger machines, computational fluid dynamics is utilized to obtain a design meeting the specifications. The pump's performance is evaluated experimentally at different rotational speeds, mass flow rates, and impeller tip clearances. The excellent agreement between experimental data and predictions from computational fluid dynamics validates the design methodology and computational results. The turbopump's characteristics are then utilized to estimate the possible performance improvement of a target organic Rankine cycle using the novel turbopump instead of a commercial multi-stage centrifugal pump. The comparison suggests that the novel turbopump increases the efficiency of the target organic Rankine cycle by 0.3 % points and decreases its back-work ratio by nearly 50 %. The novel turbopump is approximately ten times more compact compared to commercial systems.

1. Introduction

Statistics reveal that the transportation sector accounts for 29 % of carbon emissions [1]. Given that 40–50 % of the fuel energy is wasted in high-temperature exhaust gases [2], developing systems capable of recovering this waste heat can be a promising solution to improve efficiency. The organic Rankine cycle (ORC) [3-6] is among the technologies applied to exploit this waste heat. The working principle of the ORC is very similar to the Rankine cycle, in which the high-pressure working fluid is expanded to lower pressure and then condensed. The low-pressure working fluid is pumped to the evaporator and vaporized by the waste heat. The significant difference lies in the working fluid: The ORC works with organic fluids characterized by high molecular weights and low boiling pressure/temperature compared to water [7,8].

While turbines and expanders have been studied extensively [6,8,9,10], the literature is much sparser on the design and experimental investigations of the pumps for ORC applications. Meng et al. [11] studied an industrial multi-stage centrifugal pump used in a particular ORC. The pump's efficiency is reported to range from 15 % to 65.7 %, which suggests that the pump performance should be considered when developing an ORC system since poor pump efficiency reduces the thermal efficiency of the ORC. Landelle et al. [12] investigated the performance of an industrial reciprocating pump working with R134a for ORC applications. The pump was designed to work with water. However, comparable volumetric efficiencies were observed when the pump worked with R134a. Bianchi et al. [13] proposed strategies and 1-d models to design sliding vane pumps for ORC applications. Their results suggest it is crucial to consider pumping power when designing small-scale ORC systems, which is consistent with the conclusion reached by Meng et al. [11].

Yang et al. [14] experimentally investigated a multi-stage centrifugal pump for ORC applications. They suggested that higher thermal efficiency can be achieved by using an ultra-low specific speed pump. Their results also indicated that the ORC's back work ratio (BWR) depends on condensation conditions at lower pump speeds. Lei et al. [15] studied a Roto-Jet pump for a small-scale ORC system with a thermal power between 66 kW and 92 kW and an evaporating temperature between 99 °C

Nomenclature

b	channel width in meridional view, m
BWR	back work ratio
c	tip clearance, m
c	absolute velocity, m s^{-1}
d	diameter, m
H	head, m
L	length, m
$\dot{m}$	mass flow rates, kg s^{-1}
n	rotational speed, rpm
n_q	specific speed, rpm, m^{3}s^{-1}, m, $\frac{nQ^{1/2}}{H^{3/4}}$
n_{ss}	suction specific speed
p	total pressure, Pa
Q	flow rate, m^{3}s^{-1}
r	radius, m
T	temperature, K
u	peripheral velocity, m s^{-1}
w	relative velocity, m s^{-1}
$\dot{W}$	power, W
y^{+}	non-dimensional wall distance
Z	number of blades
z	axial length

Greek letters

β	flow angle,
β_B	blade angle,
ρ	density, kg m^{-3}
φ_{sp}	pitch fraction of splitter blades
ϕ	flow coefficient, $\frac{Q}{\omega r_2^3}$
π	power coefficient, $\frac{\dot{W}}{\rho\omega^3 r_2^5}$
ψ	head coefficient, $\frac{gH}{\omega^2 r_2^2}$
η	Efficiency
σ_T	THOMA's number

Subscripts

1	impeller inlet station
2	impeller outlet station
B	Blade
C	Carnot
cs	cold side
cw	cutwater
EV	evaporator
ex	exergy
i	internal
in	inlet
imp	impeller
h	hub
hs	hot side
le	leading edge
m	mean
nco	non-cavitating operation
o	outlet
opt	optimum
P	pump
r	refrigerant
s	shroud
sat	saturation
sc	subcooling
sp	splitter blades
t	total
T	turbine
th	thermal
us	useful
v	vapor

Abbreviations

1-d	1-dimensional
3-d	3-dimensional
CFD	computational fluid dynamics
NPSH	net positive suction head
ORC	organic Rankine cycle
SST	shear stress transport

and 127 °C. They reported an efficiency of between 11 % and 23 % for the pump.

Feng et al. [16] experimentally investigated an ORC system working with R245fa. The investigated pump was a multi-stage centrifugal pump. The results indicated that the isentropic efficiency of the pump varied between 12 % and 24 % under different operating conditions and heat inputs. The BWR remained almost constant for different heat inputs. However, it decreased with increasing heat input when connected to the grid. Moreover, an insignificant change in mechanical efficiency under different operating conditions was observed.

Xu et al. [17] experimentally studied the performance of a diaphragm pump for an ORC system. They reported isentropic efficiencies ranging from 57 % to 93 % depending on the working fluids and operating conditions. The results suggested that the isentropic efficiency of the pump is higher working fluids with a higher ratio of the thermal expansion coefficient to the heat capacity at constant pressure (ρc_p).

Yang et al. [18] studied a hydraulic diaphragm metering pump. They claimed that the studied ORC system could achieve higher thermal efficiency by replacing the multi-stage centrifugal pump by Meng et al. [11] with the hydraulic diaphragm metering pump. In a follow-up study, Yang et al. [19] experimentally studied and compared the performance of different pumps for an ORC system. They reported that increasing the pump's pressure rise decreases the exergy destruction rate for the multi-

stage centrifugal pump and Roto-Jet pump. On the other hand, the outlet pressure barely influences the losses or mass flow rate of the hydraulic diaphragm metering pump. They suggested that the multi-stage centrifugal pump outperforms other pumps investigated in their study. D'Amico et al. [20] developed a semi-empirical model predicting the performance characteristics of a multi-diaphragm pump for an ORC application. A good agreement was observed on the volumetric efficiency between the model's estimation and the experimental data.

Previous studies suggest that the pumping power affects the performance of the ORC system. Although researchers disagree on the appropriate pumping technology for ORC systems, some have noted the advantages of using a centrifugal pump in an ORC system. Previous studies focus primarily on commercial water pumps, which may not be an optimal solution for mobile ORC-based WHR systems. Furthermore, they are limited to evaluating the performance of commercial pumps rather than proposing methods for an efficient design and development of pumps for an ORC. Since typical working fluids for ORC have lower latent heat than water, higher mass flow rates are required to convert the same waste heat, thus increasing pump size and energy usage. The weight, size, and poor efficiency of commercial pumps that fit the specifications of typical ORC applications can depreciate the benefits of installing waste heat recovery on vehicles. Thus, efficient and smaller pumps should be developed for mobile waste heat recovery applications.

Using high-speed turbopumps in an ORC system allows for a more compact waste recovery system design compared to positive displacement pumps. However, to the knowledge of the authors, there is no study on down-scaling turbopumps to the extent of small-scale ORC systems. Hence, this work aims to present the technical feasibility of a single-stage centrifugal turbopump for ORC-based WHR applications, highlighting the importance of efficient and compact pump solutions for mobile WHR systems.

The turbopump design process heavily relies on the achieved performance of a progenitor using similarity laws. Unfortunately, the Reynolds number of industrial pumps is $10^2 – 10^3$ times higher than that of small-scale applications needed for ORC, suggesting an imperfect similarity. Consequently, using design methodology for industrial pumps may entail a risk of deviations and errors when designing a high-speed small-scale turbopump working with refrigerant working fluids. To address this issue, the hydraulic design of a small-scale high-speed turbopump suitable for an ORC system is implemented using computational fluid dynamics. Further, the pump's performances in terms of head rise, internal efficiency, useful power and total power are evaluated experimentally at different rotational speeds, mass flow rates, and impeller tip clearances. The performance of a target ORC is then calculated for the novel turbopump and is compared with a commercial multi-stage centrifugal pump.

2. Methodology

The approach in this work is split into a numerical and into an experimental part. The numerical procedure extends from the mean-line design and 1-d calculations of turbopump components to 3-d computations to improve the 1-d models for small-scale turbopumps. Finally, the design is realized and experimentally investigated to validate the numerical data. In the last step, the experimental data is utilized to evaluate the performance of an 8 kW ORC system for waste heat recovery on truck engines.

2.1. Hydraulic design and procedure of numerical analysis

The design is concerned with identifying the impeller's inlet and outlet radii, the location, and blade angle of leading and trailing edges, the meridional blade profiles, and the volute shape to satisfy the design requirements, which are the pressure rise and flow rate for a given inlet condition and working fluid. A parametric design tool developed by authors [21,22] is employed for the hydraulic design of the experimental prototype. The software enables the straightforward design and generation of turbopump geometries, which is convenient for 3-d analysis and manufacturing. The design requirements are presented in Table 1. A rotor speed of 25′000 rpm was imposed, which corresponds to a specific speed of 8.3. This constraint allows for the lowest rotational speed for the specific speed to be within the range of centrifugal pumps while preventing cavitation intensification.

Impeller. The blades are shaped radial ($\beta_{2B} = 90°$) to increase the pressure rise of the pump for a given rotational speed and outlet diameter. The optimal head coefficient, determining the impeller outlet diameter, is estimated using Eq. (1) [23]. For a given head coefficient, head rise, and rotational speed, the impeller outlet diameter can be computed with Eq. (2).

$$\psi_{opt} = 1.21 e^{-0.007713 n_q} \tag{1}$$

Table 1
Design specifications of the experimental turbopump.

Mass flow rate $\dot{m}_r(\text{kg s}^{-1})$	Pressure rise Δp (Pa)	Rotational speed n (rpm)	Specific speed n_q
0.280	20.0	25,000	8.3

$$d_2 = \frac{60}{\pi n} \sqrt{\frac{2gH}{\psi_{opt}}} \tag{2}$$

where n_s is the specific speed (dimensionless). The inlet diameter is sized for a chosen suction-specific speed ($n_{ss} = 220$). Higher values of n_{ss} result in a larger inlet diameter and better cavitation performance. However, it may cause instabilities [23]. The hub diameter is determined by the hub ratio υ, which is set at 0.35. For a given hub ratio and suction-specific speed, the inlet diameter is determined using Eq. (3) to Eq. (6)

$$d_{1,h} = \upsilon d_1 \tag{3}$$

$$k_h = 1 - \upsilon^2 \tag{4}$$

$$\tan\beta_{1d} = k_h^{1.1} \, (125/n_{ss})^{2.2} \, (n_q/27)^{0.418} \tag{5}$$

$$d_{1,s} = 2.9 \left(\frac{Q_{imp}}{n \, k_h \tan\beta_{1d}} \times \left(1 + \frac{\tan\beta_{1d}}{\tan\alpha_1} \right) \right)^{1/3} \tag{6}$$

The parameters are shown in Fig. 1. Once the inlet and hub diameters are defined, the velocity components, the flow angle, and the width (b_1) at the inlet can be determined. The blade leading edge angle can then be calculated using Eq. (7):

$$\beta_{1B} = C \tan^{-1} \beta_1 \tag{7}$$

where C is an empirical factor chosen to be 0.975 to achieve better suction performance [23]. The outlet width, b_2, is obtained by using an empirical correlation suggested by Gülich [23] as a function of the specific speed and the outlet diameter:

$$b_2 = \left[0.017 + 0.262 \left(\frac{n_q}{100} \right) - 0.08 \left(\frac{n_q}{100} \right)^2 + 0.0093 \left(\frac{n_q}{100} \right)^3 \right] d_2 \tag{8}$$

The impeller has 8 blades, which is higher than the usual number of blades (between 5 and 7) for centrifugal impellers. The blade length is smaller for radial blades and if a small number of blades is employed, the flow would be guided poorly. Utilizing splitter blades in unshrouded radial impellers may increase the pressure rise by 8 %, according to Zakeralhoseini and Schiffmann [24]. Hence, this impeller has 8 splitter blades with a length equal to 55 % of the length of the main blades and are placed in the middle of the adjacent main blades (see Fig. 2).

The meridional profiles, which are essential to generate the 3-d design of an impeller, are based on medial axis theory [21], in which the meridional shapes are built systematically for a given medial axis (see Fig. 1). The coordinates of the medial axis (r, z) are established based on a statistical model described in [21]. Then, the coordinates of
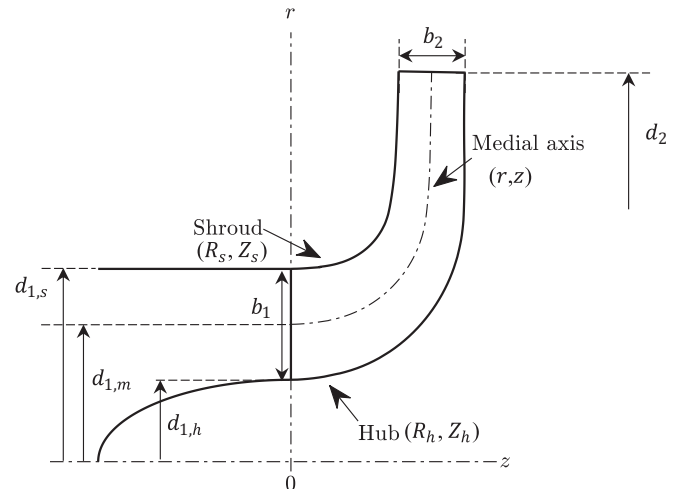

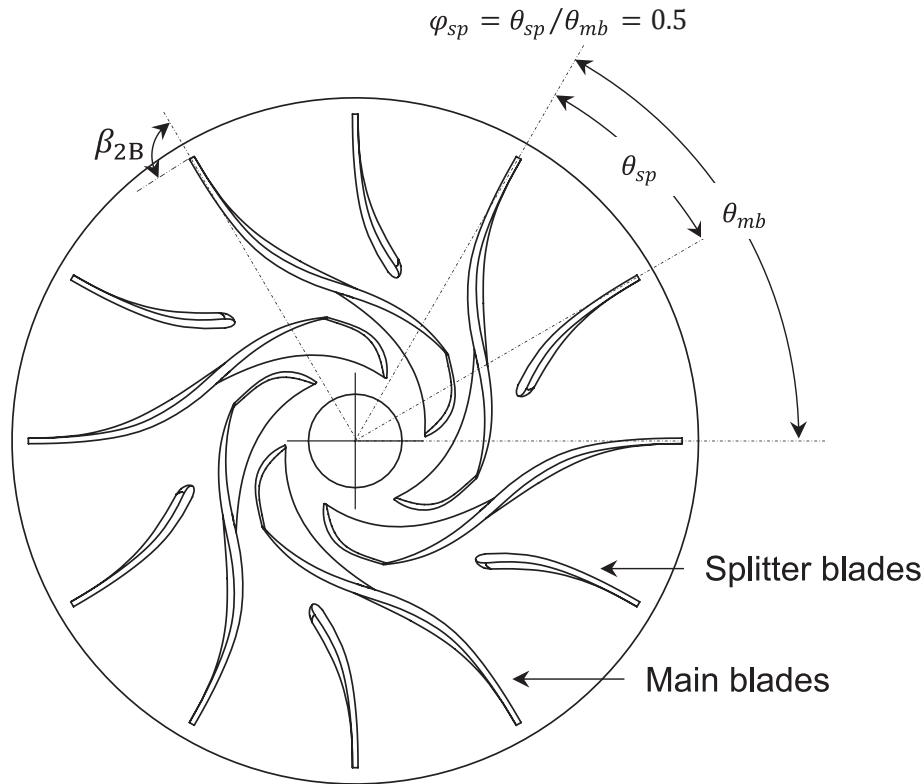**Fig. 1.** Meridional parameters and profiles.

$$\varphi_{sp} = \theta_{sp}/\theta_{mb} = 0.5$$

Fig. 2. Splitter blade parameters.

the hub (R_h, Z_h) and shroud (R_s, Z_s) profiles can be calculated for the given medial axis and a given distribution of the cross-section area. Here, the hub and shroud profiles are generated with a linear distribution of the cross-section area from the inlet to the outlet.

Once the main dimensions of the impeller and the meridional shapes are determined, the blade profiles can be obtained. The inlet diameter of the pump is designed for a relatively high suction-specific speed (n_{ss} = 220) to mitigate the cavitation. Consequently, the impeller inlet diameter increases. In such a case, it is not recommended to use 2-d blades [23,25-27], since the optimal leading-edge angle varies significantly with span. Thus, the blade is shaped 3-d at the leading edge and is tapered to a 2-d shape towards the trailing edge. The blade profiles are drawn using the method of conformal mapping. This method has been proposed by Kaplan [28]. Two parabolic curves are defined as a function of the meridional length (m) satisfying $\beta_{te} = \beta_{2B}$ and $\beta_{le,n} = \beta_{1B,n}$ with a common tangent at the intersection point representing the angle development function of the blade camber line. The sub-script n represents the span where the blade profile is drawn on.

The camber line can then be complemented with a thickness function. For each camber line, the leading edge is profiled elliptic to ensure favorable pressure distributions [23,26,29]. The transition point from the elliptical profile to the full blade thickness is 5 times the maximum blade thickness. The blade thickness gradually decreases toward the trailing edge to half of the maximum thickness to reduce pressure fluctuations. The blade is cut off at the trailing edge.

Volute. The volute design determines inlet width, cutwater diameter and position, throat area, shape, and area increment of cross-sections from the cutwater to the throat. The volute width is equal to the impeller outlet width. The cutwater is placed at a circumferential angle of $17°$ in the direction of rotation of the impeller. A clearance gap between the cutwater of the volute and the impeller is considered to maintain pressure oscillations to an allowable limit. The cutwater diameter is calculated using Eq. (9). The cutwater profile is elliptic, with a diameter determined with Eq. (10):

$$d_5 = \left[1.015 + 0.08 \left(\rho_0 H_{st} \times 10^{-6} - 0.1 \right)^{0.8} \right] \times d_4 \tag{9}$$

$$t_{cw} = 0.02\, d_2 \tag{10}$$

The volute spiral is built with rectangular cross-sections and is asymmetric for manufacturing purposes. The rectangle shape is recommended for low specific speed pumps since otherwise, the cross-sections become too large [30]. Asymmetric cross-sections are suggested to perform better than symmetrical cross-sections due to favorable secondary flow patterns [23]. The throat area is sized in agreement with Gülich's [23] recommendations. The volute cross-sections are established, assuming a constant velocity in all cross-sections over the circumference to reduce the radial forces acting on the shaft.

The main dimensions of the impeller and volute resulting from applying best engineering practices are presented in Table 2.

Table 2
Main dimensions of experimental turbopump.

| Part	Parameter	Symbol	Unit	Value
Impeller	Outlet diameter	d_2	mm	37.75
	Blade trailing edge angle	β_{2B}	°	90.0
	Outlet width	b_2	mm	1.442
	Number of main blades	Z	–	8
	Inlet diameter at the shroud	$d_{1,s}$	mm	11.59
	Inlet width	b_1	mm	3.765
	Blade length	L_B	mm	18.63
	Tip clearance	c	mm	0.100
	Blade leading edge angle	$\beta_{1B,m}$	°	10.8
	Nominal blade thickness	e	mm	0.572
	Splitter blades pitch	φ_{sp}	–	0.50
Volute	Cross-section shape	–	–	Rectangular
	Method of generation	–	–	Stepanoff
	Cutwater diameter	d_5	mm	42.00
	Cutwater circumferential angle	–	°	17.0
	Throat area	–	mm²	10.22
	Diffuser length	–	mm	40.0
	Diffuser divergence angle	–	°	5.0
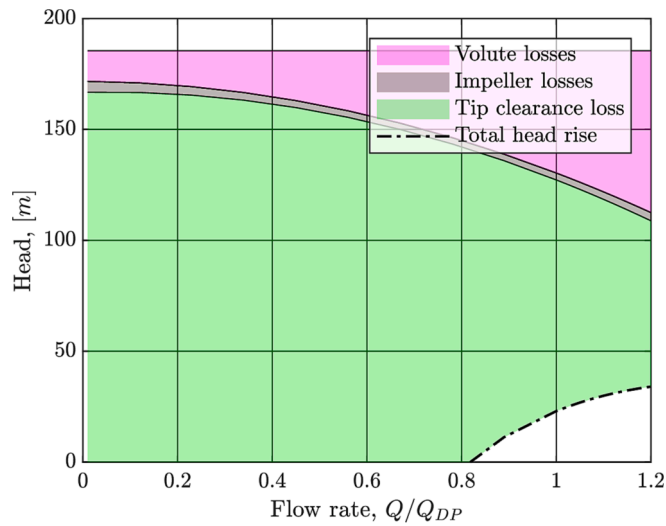
Fig. 3. Characteristic curve of the turbopump using 1-d modeling.

The turbopump's performance is approximated using reduced-order models as suggested by Gülich [23]. Referring to Fig. 3, the losses associated with the tip clearance exceed all other losses at the design point and significantly decrease the pumps' head. While a shrouded impeller is estimated to produce 126 m of head at the design point, an unshrouded impeller with a relative tip clearance of 7 % is suggested to yield a head of only 22 m. With more than 82 % of the head rise destroyed due to the tip clearance losses, it is hypothesized that the prediction of tip clearance losses with current models leads to an unrealistic performance prediction. Due to the apparent uncertainty of the 1-d estimations, the design should be further investigated with CFD analyses.

CFD analysis: The 3-d simulation is conducted to analyze the flow passing through the pump. The 3-d model of the designed turbopump is created using the design tool and is shown in Fig. 4, where they are visualized using ANSYS CFD-Post. The set-up consists of four computational domains: inlet pipe, impeller, volute, and outlet pipe.

Computational grid: The grid consists of separate volumes of the inlet pipe, impeller, volute, and outlet pipe. The structured mesh of the inlet pipe and impeller is generated with ANSYS TurboGrid. The structured mesh of the outlet pipe and the unstructured mesh of the volute are constructed using ANSYS Meshing. Several grids are generated to ensure that the CFD solutions are independent of the computational grid. First, coarse grids for the impeller and volute are generated. In the second step, the impeller grid and then the volute grid are made finer gradually so that the proper grid size of each component may be selected by comparing the results of each grid to the preceding one. A comparison of the total pressure rise and total efficiency against various grid sizes is shown in Fig. 5. The total pressure rise and the efficiency start to plateau at a grid of 9.7 million elements.

As a consequence, grids with 1 million elements for the impeller (single passage) and 8.7 million elements for the volute are selected for further steps. The properties of these grids are summarized in Table 3:

Pre-processing: Once the grids are generated, the pre-processing of domains is carried out to solve the flow field in the pump. To increase the reliability of achieved data the entire impeller is studied. The entire impeller passage is generated through rotation of the meshed single-passage domain and by adjusting boundary surfaces. Once all domains are ready, the physical properties of the working fluid and equations governing flow physics are set up in ANSYS CFX 2021R2. The simulation is carried out with R245fa as the working fluid. Its thermophysical properties in the liquid state at a temperature of 35 °C and a pressure of 6 bar are defined for the solver as summarized in Table 4.

The flow domains of the inlet conductor, volute, and outlet pipe are stationary. A rotational reference coordinate system is considered on the volume circulating in the impeller around the axis of the pump. The total inlet pressure is considered as the boundary condition at the inlet of the
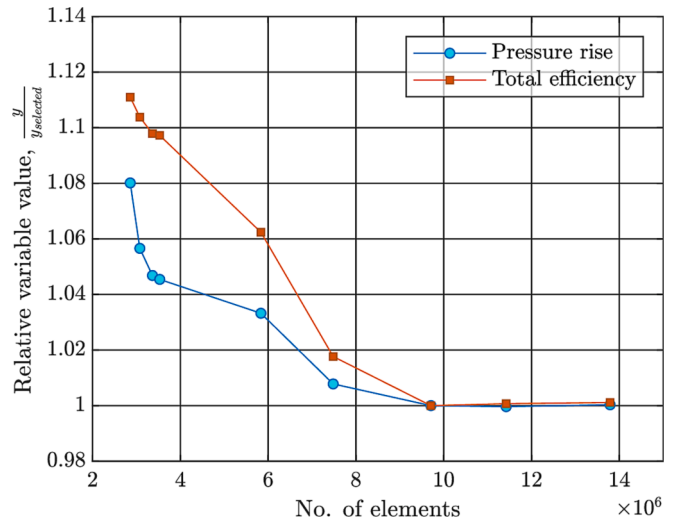

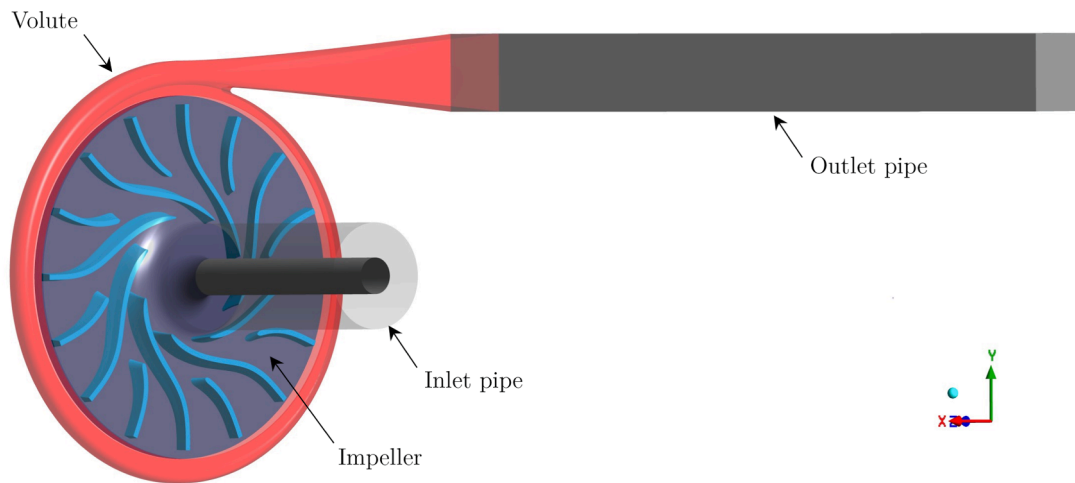**Fig. 5.** Grids independence study.

Fig. 4. Geometry of the experimental turbopump.

Table 3
Grid properties.

Domain	Property	Description
Impeller	Mesh type	Structured
	Number of elements (single passage)	1,017,570
	Minimum face angle [°]	23.96
	Maximum face angle [°]	156.04
Volute	Mesh type	Unstructured
	Number of elements	8,690,413
	Minimum face angle [°]	0.92
	Maximum face angle [°]	176.08
	Average skewness	0.2306
	The standard deviation of skewness	0.1221

pump. The relative pressure is set to 0 Pa, so the total inlet pressure is the absolute value. The mass flow rate is set as the boundary condition at the outlet of the pump giving the velocities required to solve the mathematical equations. Changing the mass flow rate varies the pump's operating point, making it possible to achieve its characteristic performance curve. The walls are treated as no-slip walls. The interface between the outlet of the impeller and the inlet of the volute is achieved by using the General Grid Interface (GGI), which allows connecting two sides of the interface with non-matching node locations. The boundary conditions are listed in Table 5.

The governing equations for the fluid flow domain are the continuity and momentum equations. The shear stress transport (SST) method [31] is used to model turbulence, and its validity is checked by using the y^+ contours. The advection terms are discretized with an upwind scheme, ensuring high accuracy with sufficient solver stability [32]. The turbulence equation is discretized with a high-resolution scheme. ANSYS CFX uses the modified Rhie and Chow [33] method of discretization to avoid decoupled pressure field and ensure the independence of the steady-state solution from the time step. In steady-state analysis, the time step acts like an accelerating guiding parameter to a physically correct solution [34]. ANSYS CFX is a coupled solver that solves the momentum terms and pressure field as a single system, reducing the number of iterations required to converge to the solution, and eliminating the necessity of selecting an appropriate relaxation factor for the system variables. [34]. The steady-state analysis is carried out using a parallel processing method on a workstation running with an AMD Ryzen processor, which has 16 logical processor cores with a frequency of 3.5 GHz. Each iteration approximately took 32.5 s on this processor.

Post-processing: Numerical calculations are carried out using ANSYS CFX-Solver. Once the domain is solved, the solution parameters are evaluated and post-processed to achieve quantitative and graphical reports on the turbopump. The validity of the turbulence model is investigated by assessing the y^+ parameter calculated from the solution.

Table 4
Thermodynamic properties of R245fa at the design point.

Molar mass	Density (kg/m³)	Kinematic viscosity (cm²/s)
134.05	1312.4	0.002692147

Table 5
Boundary conditions.

Domain	Boundary	Option
Inlet pipe	Inlet	Total pressure
	Outlet	Conformal interface
	Walls	No slip condition
Impeller	Inlet	Conformal interface
	Outlet	GGI
	Walls	No slip condition
Volute and outlet pipe	Inlet	GGI
	Outlet	GGI
	Walls	No slip condition
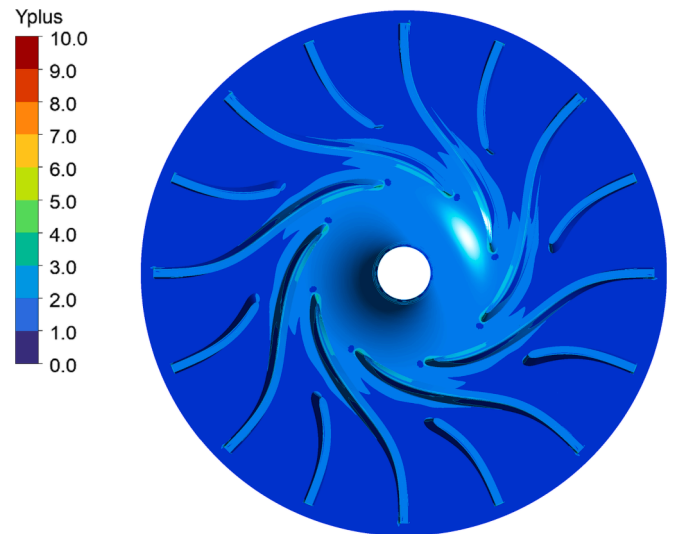
Fig. 6. The y^+ contours.

The SST model requires y^+ values of 1 to maximize the model's reliability. The post-solution y^+ contour is shown in Fig. 6.

The figure suggests that the y^+ values are below 2 almost on whole wall surfaces, highlighting the generated grids' reliability and the turbulence model's accuracy. The mean y^+ values on the hub, shroud and blade surfaces are 0.6612, 1.043, and 1.822. The maximum y^+ values are observed at the leading and trailing edges. An effort is made to achieve the lowest possible y^+ in these regions. However, a very fine grid may lead to instability and failure of the solver, which can happen due to a high accumulation of truncation errors in mesh nodes of a very fine grid.

2.2. Experimental analysis

An experimental test apparatus is designed and built to investigate the pumping stage of ORC systems. Fig. 7 shows the piping and instrumentation diagram of the experimental apparatus. The experimental apparatus is a simulative ORC system, where instead of a turbine, an expansion valve is used to expand the fluid. The test apparatus consists of an instrumented pump test section (see Fig. 8), an evaporator, a condenser, a sub-cooler, auxiliary equipment, and a data acquisition system governed by a control program. The data acquisition system connects the computer and sensors and controllers, including the spindle control unit, temperature sensors, pressure transducers, flow meters, and heating and cooling control units through the control interface developed in LabVIEW.

During the experiments, the pressure of the working fluid is raised with the experimental pump. A variable frequency drive is employed to control the pump speed. The mass flow rate is regulated with the pump speed controller and the throttle valve after the evaporator and is measured with a Coriolis-type flow meter (KROHNE CORIMASS MFM4085 10 G) after the pump. Then, the high-pressure fluid goes through an evaporator, which has been installed to maintain the system pressure within the required range. It is worthwhile to note that the idea is not to superheat the working fluid or even to reach saturated vapor but to produce enough vapor not to let the system pressure decrease. After the evaporator, the working fluid goes through the throttling valve and passes through the condenser and the sub-cooler. The sub-cooler unit is the same as the condenser unit and is employed to ensure liquid flow enters the pump. The required pressure and temperature at the inlet of the test section are achieved with careful heating and cooling balances for a given mass flow rate. The evaporator and condensers are counter-flow shell and tube heat exchangers. They are instrumented with Coriolis mass flow meters and PT1000 temperature sensors on their non-
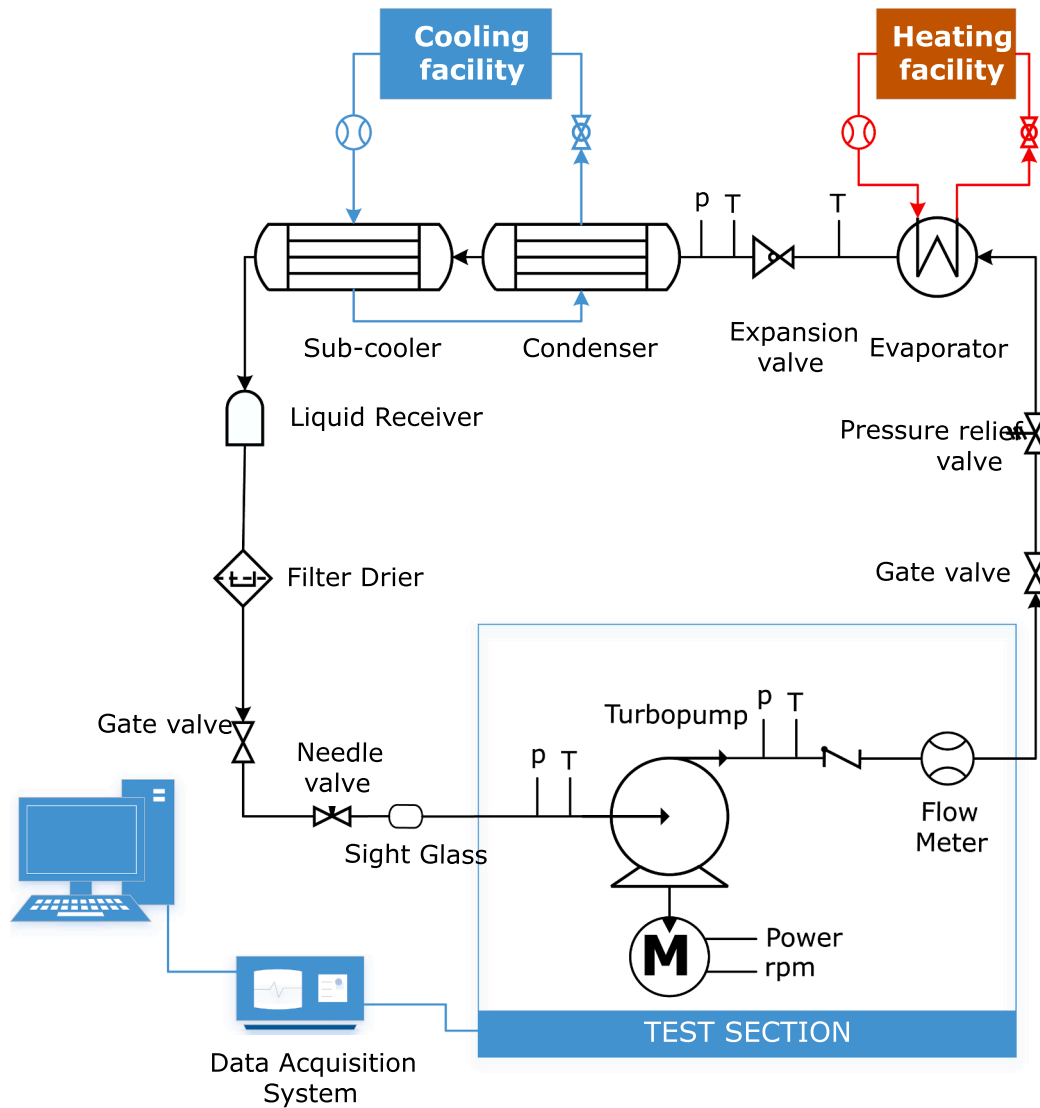
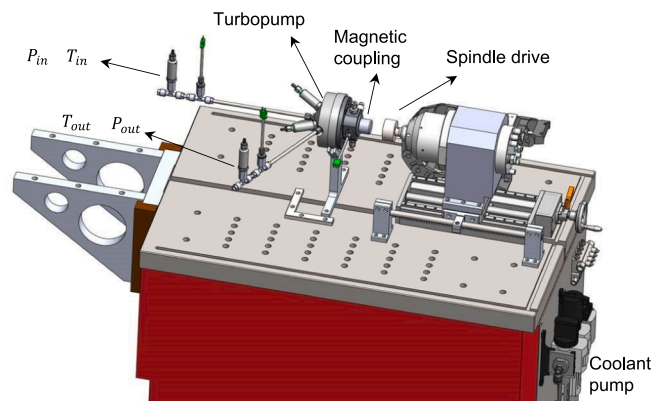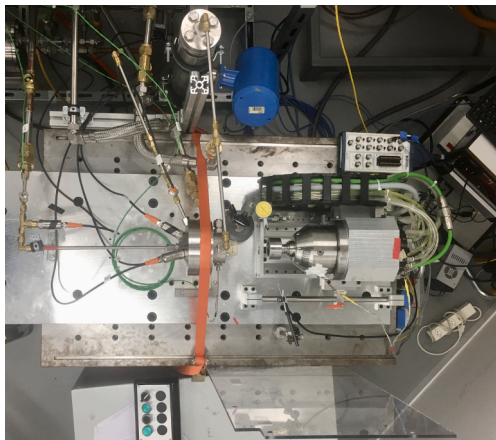**Fig. 7.** Flow diagram of the refrigerant test loop.

Fig. 8. The test section.

refrigerant sides to achieve real-time calculation of heating and cooling loads in the control program. A liquid receiver is installed vertically after the sub-cooler. It helps the system remain stable by changing the liquid level when the cooling and heating loads are changed, which improves pump suction performance. The dryer filter is employed to remove excess material and moisture, which helps to prevent frost formation in the expansion valve and to minimize chemical reactions. The sight glass is installed in the liquid line before the pump to observe the liquid level

or moisture content.

A test section, shown in Fig. 8, consists of the experimental pump, mass flow meter, pressure transmitter and temperature sensors at the inlet and outlet. The study focuses on the variation of the pump speed and mass flow rate, and their effects on the performance, including pressure rise and efficiency.

The Baumer PBMN pressure transmitters with a measuring range of 0 – 40 bar and an accuracy of 0.1 % of full scale are employed to measure refrigerant pressure. They are absolute-type pressure transmitters with an output signal of 0 – 10 V. PT1000 temperature sensors with an accuracy of 0.1 °C and a diameter of 6 mm are used to measure the temperature of the working fluid, condenser coolant and evaporator heating oil. Auxiliary temperature measurements such as oil tank temperature are achieved with a K-Type thermocouple with an accuracy of 1 °C.

The temperature data are logged using a Keysight 34901A multiplexer. The module has a built-in thermocouple reference junction. It can scan different thermocouples, two- and four-wire resistance (e.g., PT1000), and ac/dc volts simultaneously, making it a proper solution due to the different sensor characteristics of the current study. The module is installed within the Keysight 34970A data acquisition/switch unit. The data from pressure sensors and mass flow meters is digitalized using modules of NI 9205 and NI 9203, respectively, which are governed by NI cRIO 9074 controllers. The NI 9205 module provides high-accuracy measurements of the analog signal of ± 10 V, and the NI 9203 module is an 8-channel digitizing the current analog signal of $0mA$ to $20mA$. A high-speed data link between the turbopump drive and controller is established through a KUNBUS ProfiBus DP module. The turbopump drive is a 35-kW spindle developed by IBAG Motor Spindles. The spindle is shipped with the LTi drive manager for programming the drive and its I/O channels. The LTi drive controller is programmed to communicate the rotational speed control and feedback signals through the ProfiBus DP module.

The pump itself is linked to a preloaded ball bearing supported rotor. The bearings are lubricated with subcooled liquid phase working fluid. The hermetic system is driven by the electric spindle through a magnetic coupling.

The procedure of experiments: Initially, the heating and cooling facilities are started. Once the heating oil reaches the set temperature, it flows inside the evaporator to vaporize the refrigerant liquid and increase system pressure. The coolant is supplied to the condenser to ensure the pump sucks liquid refrigerant upon its start. As soon as the pressure reaches a safe level, providing enough margin to prevent cavitation, the pump is switched on while the expansion valve is fully open. At each rotational speed, the expansion valve is closed gradually to reduce the refrigerant mass flow rate and to achieve performance maps as functions of rotational speed and mass flow rate. The data are logged when the system reaches steady-state conditions.

3. Data reduction method

The experiments are carried out for the parameter ranges listed in Table 6. MATLAB [35] and REFPROP [36] are embedded in the developed LabVIEW interface to evaluate the thermophysical properties of the working fluid and to post-process the experimental data in real-time. The repeatability of the experiments is validated by repeating the experiments and reproducing the results at different ranges of parameters.

3.1. Pump performance

Given temperatures (T_{in}, T_o) and pressures (P_{in}, P_o) at the inlet and outlet of the pump, specific enthalpies (h_{in}, h_o) and densities (ρ_{in}, ρ_o) are calculated. The flow rate and head rise produced by the pump are calculated based on the average density of the flow passing through the pump. The flow rate and head rise are calculated as follows:

$$Q_r = \frac{\dot{m}_r}{\rho_r} \tag{11}$$

$$H = \frac{p_o - p_{in}}{\rho_r g} \tag{12}$$

where $\dot{m}_r$ is the mass flow rate of the working fluid, and ($p_o - p_{in}$) the pressure rise produced by the pump. Similarly, the saturation pressure (p_{sat}) and temperature (T_{sat}) for a given temperature (T_{in}) and pressure (P_{in}) at the pump's inlet are calculated. Once the saturation properties are calculated, the subcooled temperature and pressure are calculated as follows:

$$\Delta T_{sc} = T_{sat} - T_{in} \tag{13}$$

$$\Delta p_{sc} = p_{in} - p_{sat} \tag{14}$$

The subcooled temperature and pressure are monitored to maintain a sufficiently high cavitation margin. Once the pressure rise of the pump and the flow rate are calculated, the useful power given to the flow is computed as follows:

$$\dot{W}_{us} = (p_o - p_{in}) Q_r \tag{15}$$

The total power given to the flow, which accounts for the internal and heat losses, can be calculated based on the enthalpy rise of the flow passing through the pump:

$$\dot{W}_t = \dot{m}_r (h_o - h_{in}) \tag{16}$$

Therefore, the internal efficiency of the pump can be computed with Eq. (17):

$$\eta_i = \frac{\dot{W}_{us}}{\dot{W}_t} \tag{17}$$

Unfortunately, the measurement of the torque acting on the shaft or the total power required to turn the shaft is not possible due to the magnetic coupling between the turbopump shaft and the spindle drive.

3.2. Uncertainty analysis

Instruments are calibrated for the range of parameters listed in Table 6. The uncertainties of computed quantities are calculated based on the error propagation method proposed by Moffat [37]. The uncertainties of measured and calculated variables are summarized in Table 7:

The influence of each measured quantity on the efficiency uncertainty is calculated and summarized in Table 8 for a given operating point. As can be seen, the temperature measurements at the inlet and outlet of the pump have the most significant effect on the uncertainty, as

Table 6
Experimental conditions.

Parameter	Saturation Temperature T_{sat} (°C)	Subcooling pressure p_{sc} (bar)	Mass flow rate m (g s^{-1})	Pressure rise Δp (bar)
Range	5 – 20	2 – 7	0 – 333	4 – 25

Table 7
Uncertainties of the measured and computed variables.

Variable	Uncertainty
Temperature	± 0.1 °C
Refrigerant mass flow	± 0.15 % of the measured value
Absolute pressure	± 0.1 % of the measuring range
Head rise	± 0.29 %
Useful work	± 0.36 %
Total work	± 8.17 %
Internal efficiency	± 8.32 %

they contribute to 92.5 % of the efficiency uncertainty.

3.3. ORC characteristics

In the last evaluation step, the performance of the tested turbopump is blended into an experimental regenerative ORC system running with a small-scale, high-speed, lubricant-free turbine [38,39]. The flow diagram and (T,s) diagram of a regenerative ORC system are shown in Fig. 9 and Fig. 10, respectively.

Initially, the ORC system ran with a multi-stage centrifugal pump with a maximum rotational speed of 3000 rpm to flow the refrigerant at the required pressure in the cycle. The pump is a 27-stage vertical model from Grundfos (CRNE 1–27), and it is connected by flanges to inlet and outlet pipes in the ORC system test apparatus, as shown in Fig. 11. The pump is driven by a 3-phase synchronous motor and includes a built-in frequency converter to control its rotational speed.

The experimental results achieved for the developed small-scale pump are characterized by tabular data of the experimental head rise and power against its capacity (flow rate). Then, the pump's performance for any operating points of the ORC system is determined from similarity laws using the given reference tabular data. Three efficiencies are defined to compare the performance of the ORC driven by the commercial multi-stage pump and the developed single-stage turbopump:

The back-work ratio (BWR) is defined as the fraction of the electrical power that the turbine generates, which is consumed by the pump. The BWR is given as follows:

$$BWR = \frac{\dot{W}_P}{\dot{W}_T} \tag{18}$$

In this study, the pump's electrical input power is unavailable. Thus, the BWR is calculated with the total power (Eq. (16)) given to the flow:

$$BWR = \frac{\dot{m}_r \left(\dot{h}_2 - \dot{h}_1 \right)}{\dot{W}_T} \tag{19}$$

The thermal efficiency is the fraction of the heating energy the working fluid absorbs, which is converted to net power. For the ORC system in Fig. 9, the thermal efficiency is given as follows:

$$\eta_{th} = \frac{\dot{W}_{net}}{\dot{Q}_h} = \frac{\dot{W}_T - \dot{W}_P}{\dot{Q}_h} \tag{20}$$

Similar to the BWR, the total power given to the flow (Eq. (16)) is used to determine the thermal efficiency as below:
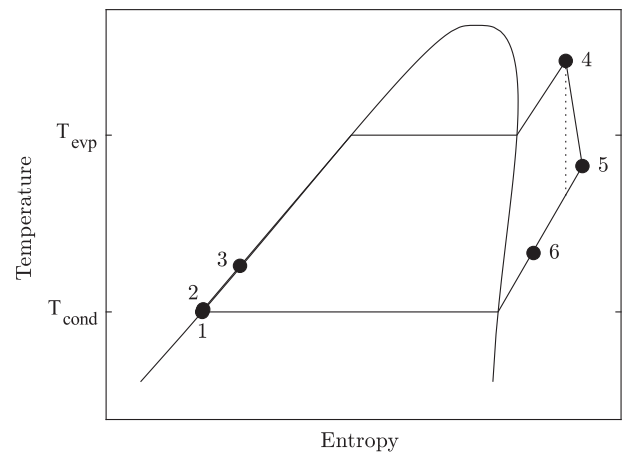
Table 8
The influence of measurement uncertainty on the uncertainty of the efficiency.

Quantity	Value	Uncertainty	Uncertainty contribution
Inlet temperature	6.9 °C	±0.1 °C	48.67 %
Outlet temperature	11.9 °C	±0.1 °C	48.44 %
Inlet pressure	5.45×10^5 Pa	$\pm 2 \times 10^3$ Pa	1.46 %
Outlet pressure	21.49×10^5 Pa	$\pm 2 \times 10^3$ Pa	1.43 %
Mass flow rate	231.24×10^{-3} kg/sec	$\pm 0.17 \times 10^{-3}$ kg/sec	~0 %

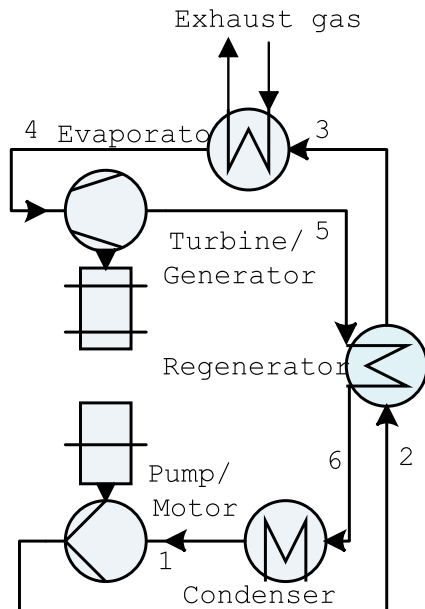**Fig. 10.** (T,s) diagram of a regenerative ORC.

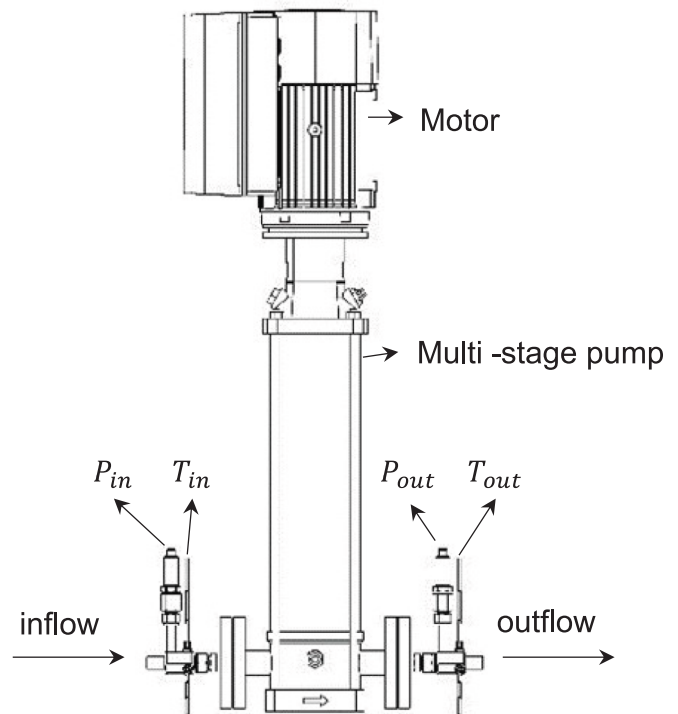**Fig. 9.** Flow diagram of a regenerative ORC diagram.

Fig. 11. Schematic of the test section for the multi-stage centrifugal pump.

$$\eta_{th} = \frac{\dot{W}_T - \dot{W}_{P,t}}{\dot{Q}_h} = \frac{\dot{W}_T/\dot{m}_r - \left(\dot{h}_2 - \dot{h}_1\right)}{\dot{h}_4 - \dot{h}_3} \tag{21}$$

The exergy efficiency is defined as the ratio of the thermal efficiency to the Carnot efficiency [39]:

$$\eta_{ex} = \frac{\eta_{th}}{\eta_C} \tag{22}$$

where Carnot efficiency (η_C) is evaluated as below [39]:

$$\eta_C = 1 - T_{cs,\ in} \frac{\ln\left(\frac{T_{hs,\ in}}{T_{hs,\ o}}\right)}{T_{hs,in} - T_{hs,\ o}} \tag{23}$$

4. Results and discussion

4.1. Pump performance characteristics

Fig. 12 presents the performance characteristics of the experimental pump running at 25,000 rpm at different capacities for tip clearances of 100 μm, 200 μm and 400 μm. The non-dimensional parameters of the

flow coefficient, head coefficient and power coefficient are given in Eq. (24) to Eq. (26):

$$\phi = \frac{Q}{\omega r_2^3} \tag{24}$$

$$\psi = \frac{gH}{\omega^2 r_2^2} \tag{25}$$

$$\pi = \frac{\dot{W}}{\rho \omega^3 r_2^5} \tag{26}$$

The figure suggests that the head coefficient (Fig. 12, a) changes slightly with the flow coefficient (capacity). According to the Euler equation of turbomachinery, the head characteristic curve is independent of the flow rate for radial blades ($\beta_{2,B} = 90°$). However, as the tip clearance increases, the head coefficient decreases from above 0.6 to less than 0.525. On the other hand, the total power (Fig. 12, d) remains constant for different tip clearances. Therefore, the efficiency drops (Fig. 12, b) with increasing tip clearances.

Validation of CFD analysis: Fig. 13 compares the characteristics curves of the head rise, power, and efficiency against pump capacity
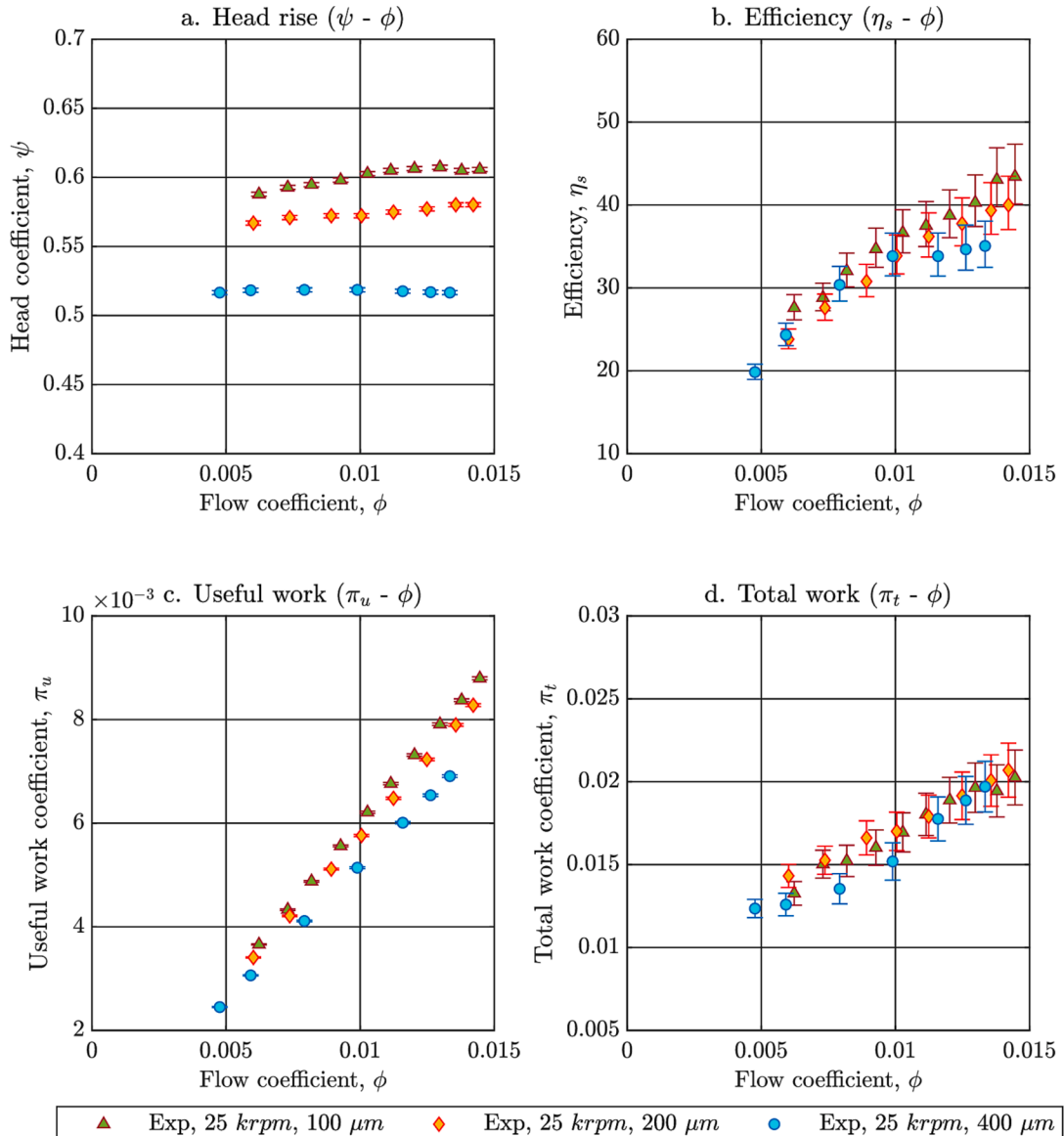

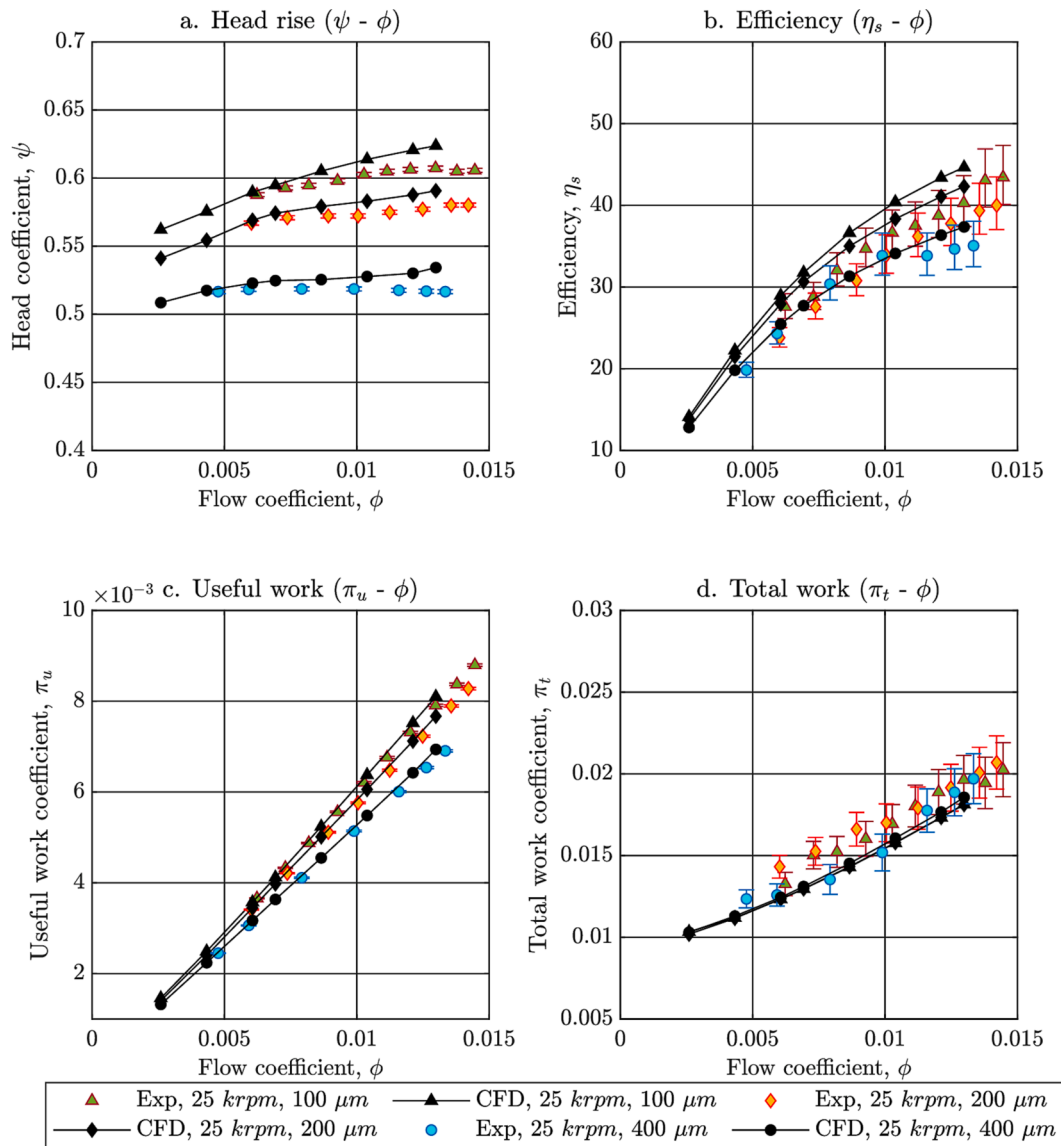**Fig. 12.** Experimental performance characteristics of the turbopump at different tip clearances.

Fig. 13. Comparison between experimental and numerical characteristics against flow coefficient at different tip clearances.

between experimental results and CFD data at different tip clearances for a rotational speed of 25,000 rpm.

The figure suggests a good agreement between the experimental results and CFD data. The maximum deviation of the head coefficient predicted with CFD analysis is 3.51 % at a tip clearance of 400 μm, highlighting the reliability of the CFD analysis carried out on the small-scale turbopump. At a tip clearance of 400 μm, the maximum deviations of the usable work, total work, and internal efficiency predicted using the CFD data are 1.78 %, 14.02 %, and 16.40 %, respectively. The CFD results deviate within the measurement uncertainty range, even though the CFD errors are higher for the predictions of total work and internal efficiency. The higher uncertainty in the calculation of total work and internal efficiency stems from the measurement errors in the temperature.

Fig. 14 shows the effect of tip clearance on the flow pattern represented by the velocity vectors of the flow through the impeller and volute at mid-span. The velocity vectors in the impeller are relative to the rotating frame of reference (w/u_2) and are colored by the flow's normalized absolute velocity (c/u_2). The figure suggests that the flow pattern inside the impeller is strongly affected by the increasing tip clearance. A strong jet flow is created at the suction side of the main blade, which, as a result, intensifies the wake region in the flow passage.

The secondary flows and the wake region's intensification increase the impeller's hydraulic losses and, as a result, reduce the head rise of the pump and decrease its efficiency.

Effect of rotational speed: The characteristic curves of the pump are calculated both experimentally and with CFD at different rotational speeds for different tip clearances. The curves of the head coefficient against the flow coefficient calculated with CFD at the rotational speeds of 25,000 rpm (circles) and 30,0000 rpm (squares) for tip clearances of 100 μm, 200 μm and 400 μm are represented in Fig. 15. Fig. 16 shows the same characteristic curves based on experimental data.

The data suggest that increasing the tip clearance reduces the head coefficient and efficiency. However, at each tip clearance, the pump characteristics still follow the similarity, since the results for different rotor speeds collapse to the same curves. The similarity laws imply that the non-dimensional characteristics of all similar pumps i.e. pump belonging to the same family match. Once the non-dimensional characteristics of a family are determined, characteristics of any other pump belonging to that family, which its diameter and rotational speed are specified can be derived. It is sufficient two determine two properties, such as $\psi = f(\phi)$ and $\eta_i = f(\phi)$ since non-dimensional parameters are related to each other:
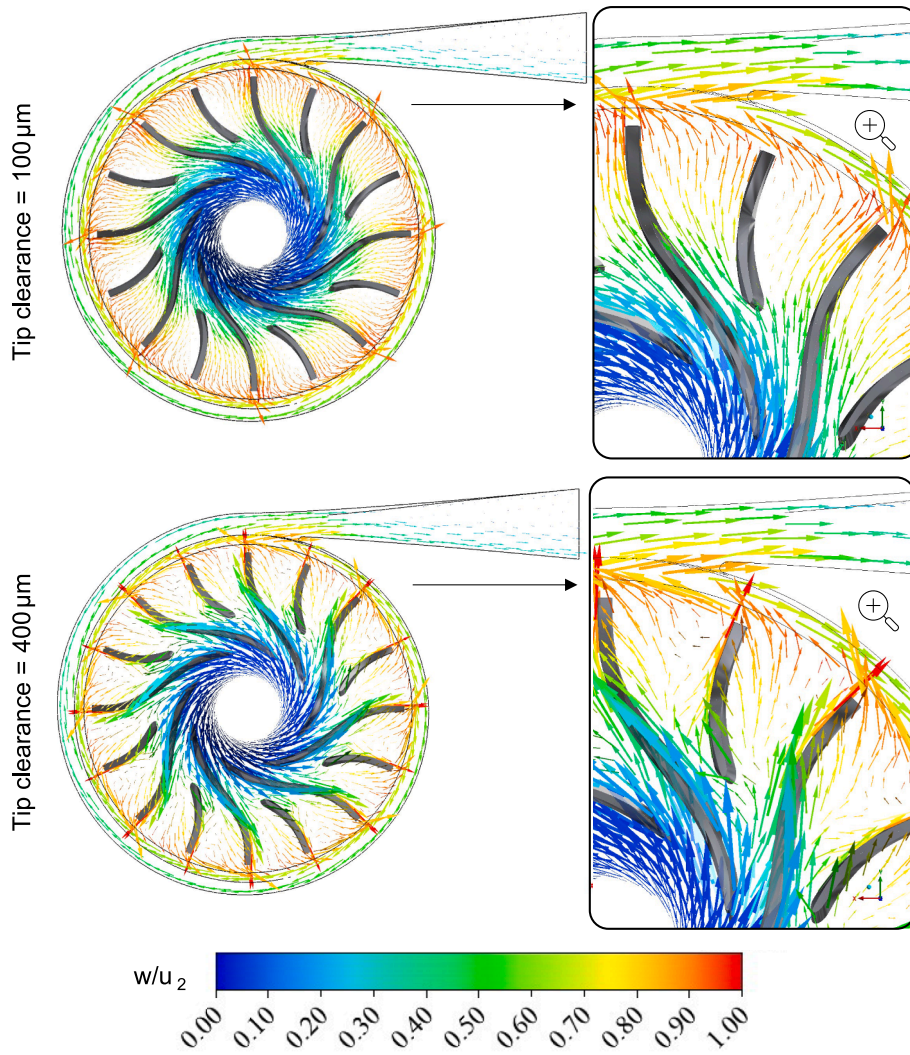
Fig. 14. Contours of normalized velocity (w/u_2) colored by absolute velocity value (c/u_2) at mid-span ($n = 25{,}000$ rpm, $\phi = 0.012$).
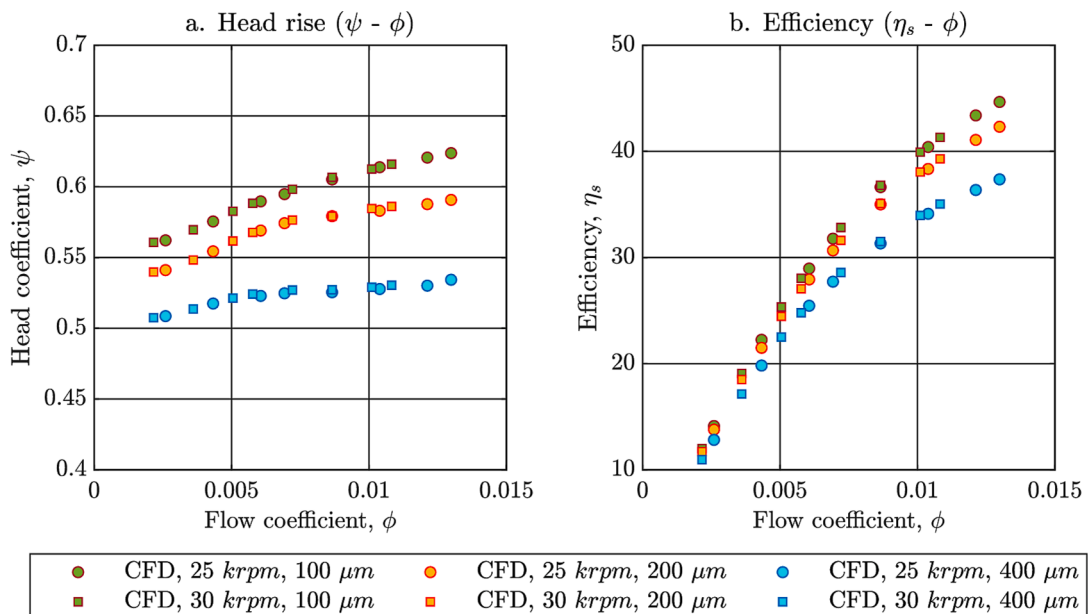

Fig. 15. The characteristic curve of head coefficient and efficiency against flow coefficient achieved with CFD at different rotational speeds and tip clearances.
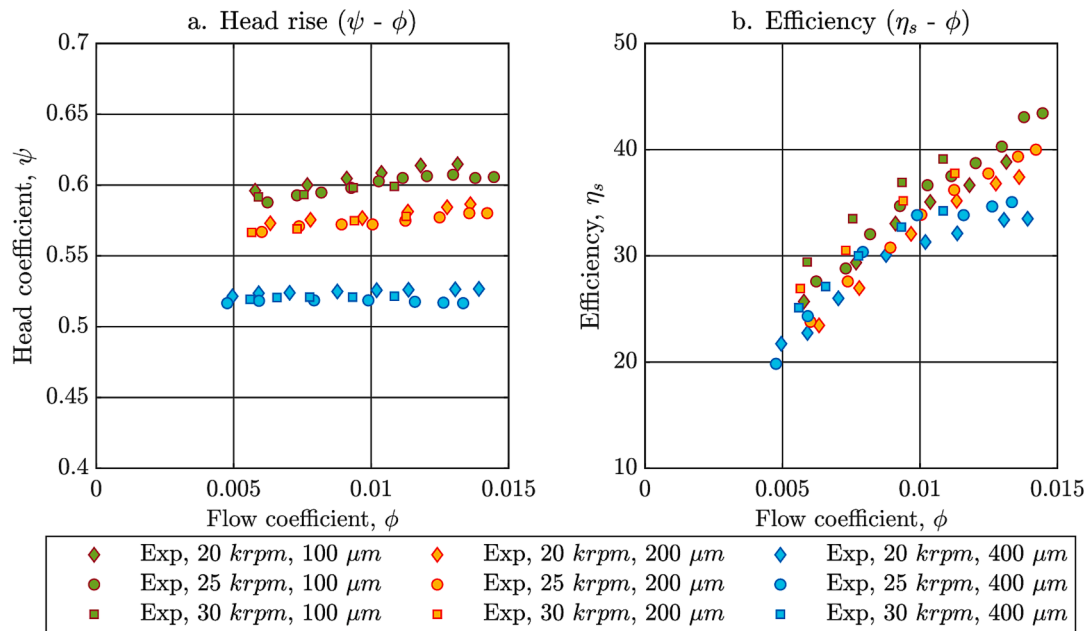
Fig. 16. The characteristic curve of experimental head coefficient and efficiency against flow coefficient at different rotational speeds and tip clearances.

$$\pi = \frac{\psi\phi}{\eta_i} \quad (27)$$

If the characteristic curves of a pump for a specific rotational speed are available, its characteristic curves can be determined for any other required rotational speed by employing similarity rules. If a rotational speed of a pump changes from n_A to n_B, the new operating point of a pump can be determined by mapping the head and flow rate of current operating point A as follows:

$$H_B = \left(\frac{n_B}{n_A}\right)^2 H_A \quad (28)$$

$$Q_B = \left(\frac{n_B}{n_A}\right) Q_A \quad (29)$$

According to similarity laws, points A and B will have the same efficiency. Therefore, the new characteristic curve can be determined and plotted on the head-discharge map. Fig. 15 and Fig. 16 suggest that the fundamental similarities between head rise, flow, and internal power continue to apply to unshrouded impellers. In addition, matched dimensionless characteristics at different rotational speeds suggest the CFD analysis's stability and reliability on the whole pumping stage.

4.2. Cavitation margin

Cavitation is a complex phenomenon, which is out of the scope of this paper to review it in detail, and only a preliminary evaluation to prevent it will be summarized. The cavitation sets the allowable suction head of the pumps, and is evaluated by employing THOMA's number [26] defined by the following equation:

$$\sigma_T = \frac{NPSH}{H} \quad (30)$$

where *NPSH* is the net positive suction head parameter representing the total flow energy of the flow in the suction pipe before the occurrence of cavitation as defined below:

$$NPSH = \frac{p_1 - p_v}{\rho g} + \frac{c_1^2}{2g} \quad (31)$$

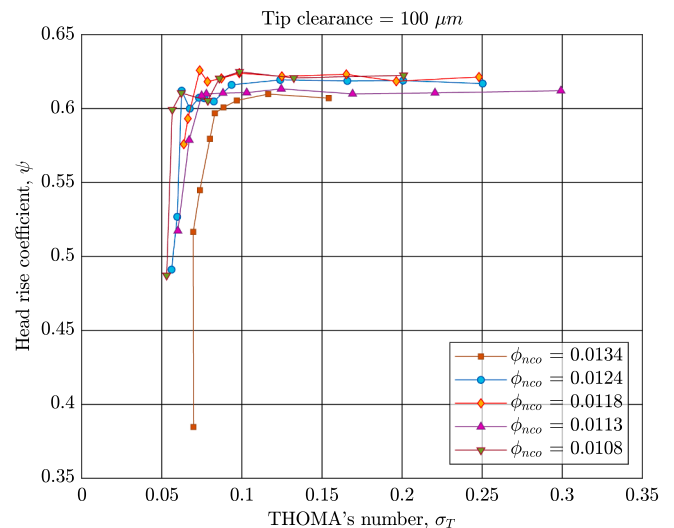where p_v is the vapor pressure at the inlet temperature. In cavitating

Fig. 17. Head rise coefficient at different THOMA's numbers (σ_T) and flow coefficients (at non-cavitating operation).

flow for a given mass flow rate, at a particular value of NPSH or THOMA's number, the overall performance of a machine will be destroyed due to the cavitation surge. Thus, the minimum energy required in the suction pipe of the pump to prevent cavitation is defined as a required (critical) NPSH, where the velocity and pressure of the cavitation threshold are applied in Eq. (31). Hence, any higher value of available NPSH corresponds to a safe margin of machine operation.

Fig. 17 represents the experimentally measured head rise coefficient achieved by the turbopump rotating at 25,000 rpm at a tip clearance of 100 μm as a function of THOMA's number (σ_T) for different flow coefficients (at non-cavitating operation, ϕ_{nco}). The figure suggests that the pump can operate with a safe margin against cavitation for any THOMA's number (σ_T) higher than 0.1 for all flow coefficients. The critical THOMA's number (σ_T) at which the pump's head rise is destroyed due to the cavitation surge, varies between 0.05 and 0.1 depending on the pump flow coefficient.
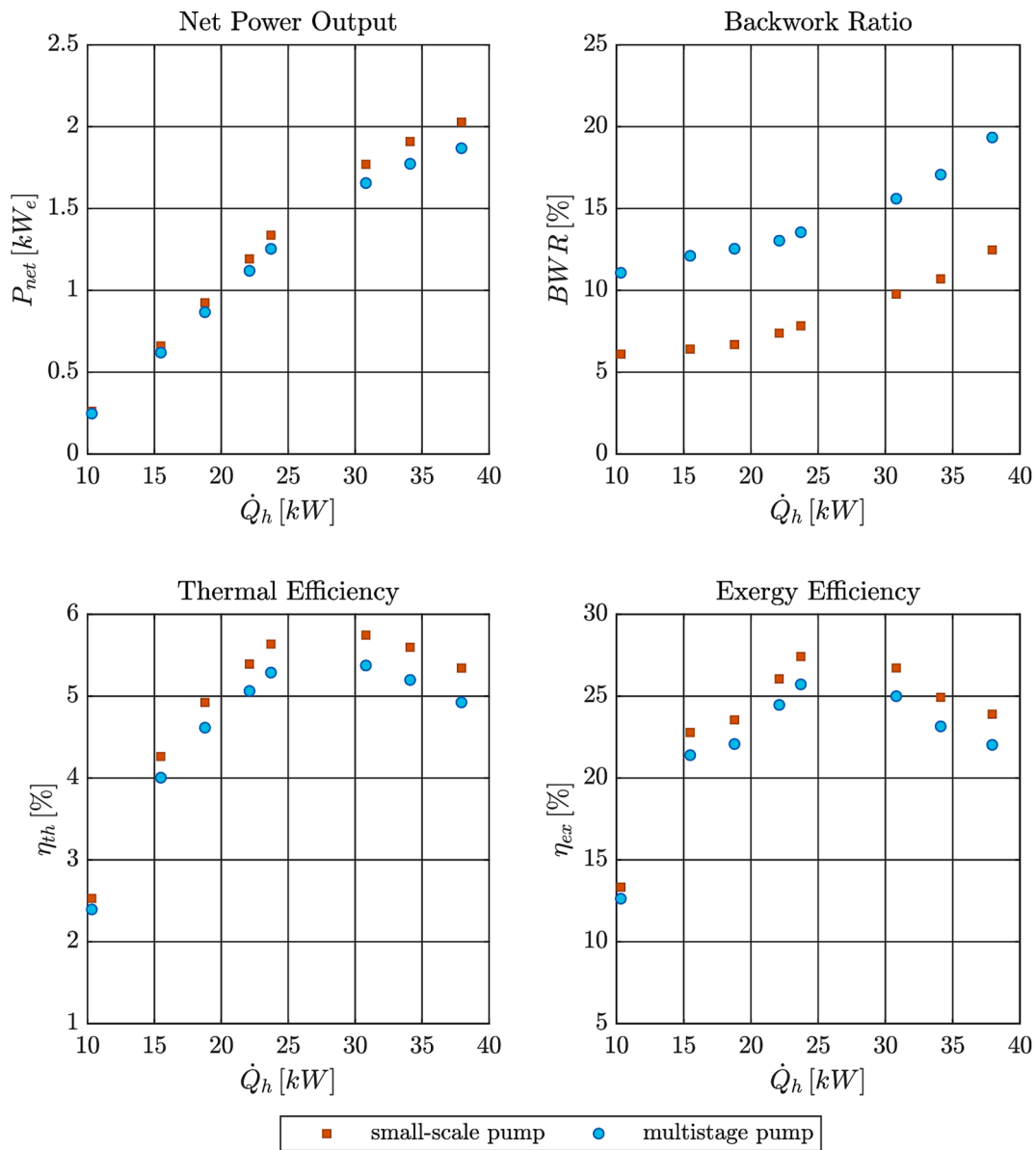
Fig. 18. Comparison of performance characteristics for the target ORC system.

4.3. ORC characteristics

Fig. 18 relates the performance characteristics of the targeted ORC system running with a small-scale radial inflow turbine using the small-scale turbopump of this study in comparison with the original multi-stage centrifugal pump. The performance characteristics are evaluated using the total power delivered to the flow for both pumps. The comparison clearly suggests that the use of the small-scale turbopump increases the net power output of the ORC system by 13 W to 160 W. The BWR of the system decreases by up to 6.8 % of the generator's output power and is reduced by nearly 50 % compared to the commercial pump. Fig. 18 (c and d) suggests that a mean increase of 0.32 % points and 1.52 % points can be anticipated for the thermal and exergy efficiency, respectively, if the small-scale turbopump is employed for the ORC system instead of the commercial multi-stage pump.

Fig. 19 shows the effect of the tip clearance of the small-scale turbopump on the performance characteristics of the ORC system. As made clear in Fig. 12, the pump efficiency drops with increasing the tip clearance. Thus, more power is required for a given pressure rise of the working fluid. Consequently, the BWR of the ORC system is anticipated

to increase with increasing the tip clearance. Fig. 19 (b) confirms that by increasing the tip gap from 100 μm to 400 μm, the BWR of the ORC system decreases by 1 % of the net power of the generator. Thermal efficiency also decreases with increasing the tip clearance. However, its influence is insignificant (0.06 % of the input heat power) as the range of the input heat power is two orders of magnitude higher than the change of the pumping power with the tip clearance.

5. Conclusions

A small-scale high-speed turbopump with a rectangular axisymmetric volute and an unshrouded impeller with a tip diameter of 37.75 mm, with 8 radial blades and splitters is designed for ORC-based waste heat recovery applications on truck engines. The turbopump is examined numerically and experimentally to evaluate its performance characteristics and investigate its influence on the performance of the ORC system. The work presented here highlights the technical feasibility of a single-stage turbopump for driving organic Rankine cycles with a net output power in the order of 10 kWel, and underlines the importance of efficient and compact pump solutions for driving organic Rankine
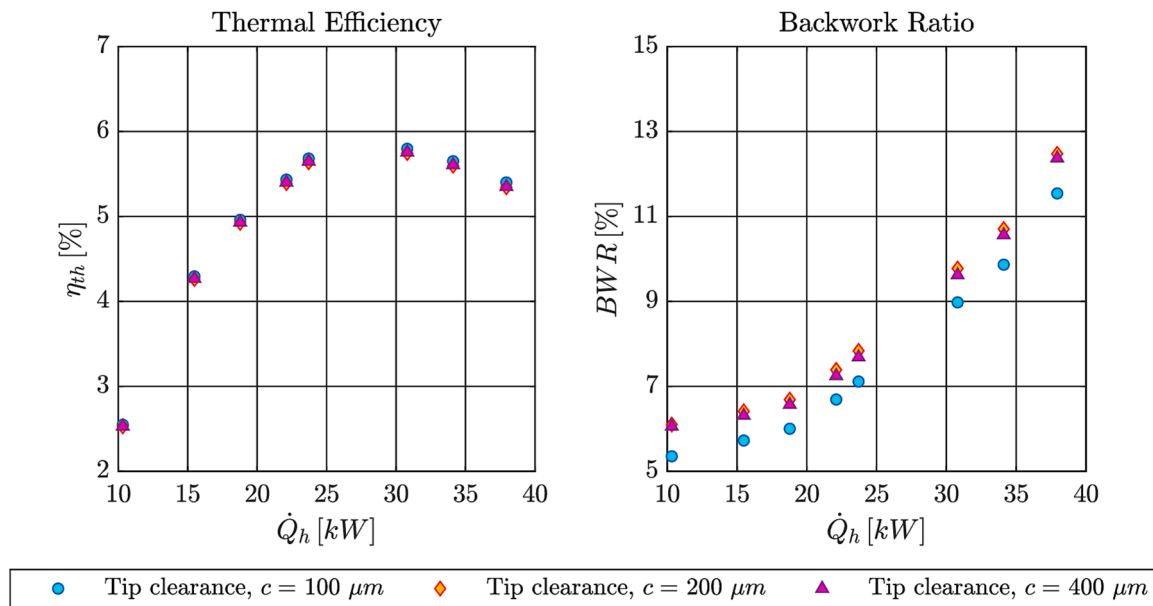
Fig. 19. The influence of tip clearance on the performance characteristics of the ORC system.

cycles. Further, the underlying methods to efficiently design small-scale turbopumps working with refrigerants are presented, emphasizing that the CFD analysis can be employed to facilitate the design process of such out of the common machines. The key findings are summarized as follows:

1. 14. Using 1-d models without further 3-d analysis may lead to improper geometric parameters and unreliable performance estimation for small-scale unshrouded pumps.
2. 15. The head coefficient and useful work of the pump decrease with increasing tip clearance, and the pump's efficiency decreases.
3. 16. Compared to a commercial 27-stage pump, the designed single-stage pump is suggested to increase the ORC thermal and exergy efficiency by 6.8 %, while reducing the BWR by 41.5 %.
4. 17. As the tip clearance of this investigated single-stage turbopump increases from 100 μm to 400 μm, the thermal efficiency of the ORC is expected to decrease slightly while the BWR increases by roughly 1 % of the generator's output power.

With the emerging application of small-scale turbopumps in ORC systems, the study on deviations of small-scale turbopumps compared to large industrial pumps and their influence on the performance of ORC systems will become increasingly important. This study is one of the first on developing an efficient and compact turbopump for ORC systems, which opens exciting possibilities for future research. This study is limited to a turbopump with a specific speed of 8.9, while other specific speeds may be required for alternative specifications. Turbopumps with higher specific speeds offer benefits such as smaller dimensions, but yield drawbacks such as lower cavitation margin due to higher speeds and flow velocities. Therefore, more small-scale turbopumps would have to be designed and experimentally investigated to assess the properties at varying specific speeds. Moreover, the results of this investigation suggest that the tip clearance ratio is a critical parameter for the performance of such machines. Even though its influence on performance characteristics is evaluated in this study, the underlying mechanism behind its influence remains unknown. Experiments coupled with CFD-based analysis could be carried out to understand the fundamental mechanism of tip leakage flow in small-scale turbopumps and their effects on performance.

CRediT authorship contribution statement

Sajjad Zakeralhoseini: Conceptualization, Methodology, Software, Validation, Formal analysis, Investigation, Resources, Writing – original draft, Visualization. **Jürg Schiffmann:** Supervision, Project administration, Writing – review & editing.

Declaration of Competing Interest

The authors declare that they have no known competing financial interests or personal relationships that could have appeared to influence the work reported in this paper.

Data availability

Data will be made available on request.

References

[1] "2015 Chicago Regional Greenhouse Gas Emissions Inventory," Jun. 2018. Accessed: Mar. 04, 2022. [Online]. Available: https://www.cmap.illinois.gov/documents/10180/885293/2015+Chicago+Regional+Inventory_Final+Report_June+2018.pdf/.

[2] Serrano D, et al., Improving train energy efficiency by Organic Rankine Cycle (ORC) for recovering waste heat from exhaust gas. In: *3rd international seminar on ORC power systems*, 2015.

[3] Quoilin S, van den Broek M, Declaye S, Dewallef P, Lemort V. Techno-economic survey of organic rankine cycle (ORC) systems. Renew Sustain Energy Rev 2013. https://doi.org/10.1016/j.rser.2013.01.028.

[4] Capata R, Toro C. Feasibility analysis of a small-scale ORC energy recovery system for vehicular application. Energy Convers Manag 2014;86:1078–90.

[5] Rahbar K, Mahmoud S, Al-Dadah RK, Moazami N, Mirhadizadeh SA. Review of organic Rankine cycle for small-scale applications. Energy Convers Manag 2017; 134:135–55.

[6] Dai Y, Wang J, Gao L. Parametric optimization and comparative study of organic Rankine cycle (ORC) for low grade waste heat recovery. Energy Convers Manag 2009;50(3):576–82.

[7] Rahbar K, Mahmoud S, Al-Dadah RK, Moazami N, Mirhadizadeh SA. Review of organic Rankine cycle for small-scale applications. Energy Convers Manage 2017. https://doi.org/10.1016/j.enconman.2016.12.023.

[8] Bao J, Zhao L. A review of working fluid and expander selections for organic Rankine cycle. Renew Sustain Energy Rev 2013;24:325–42.

[9] Mounier V, Olmedo LE, Schiffmann J. Small scale radial inflow turbine performance and pre-design maps for Organic Rankine Cycles. Energy 2018;143: 1072–84.

[10] Mounier V, Mendoza LC, Schiffmann J. Thermo-economic optimization of an ORC driven heat pump based on small scale turbomachinery and comparison with absorption heat pumps. Int J Refrig 2017;81:96–110.

[11] Meng F, et al. Study of efficiency of a multistage centrifugal pump used in engine waste heat recovery application. Appl Therm Eng Jan. 2017;110:779–86. https://doi.org/10.1016/j.applthermaleng.2016.08.226.

[12] Landelle A, Tauveron N, Revellin R, Haberschill P, Colasson S, Roussel V. Performance investigation of reciprocating pump running with organic fluid for organic Rankine cycle. Appl Therm Eng Feb. 2017;113:962–9. https://doi.org/10.1016/j.applthermaleng.2016.11.096.

[13] Bianchi G, Fatigati F, Murgia S, Cipollone R. Design and analysis of a sliding vane pump for waste heat to power conversion systems using organic fluids. Appl Therm Eng 2017;124:1038–48. https://doi.org/10.1016/j.applthermaleng.2017.06.083.

[14] Yang Y, Zhang H, Tian G, Xu Y, Wang C, Gao J. Performance Analysis of a Multistage Centrifugal Pump Used in an Organic Rankine Cycle (ORC) System under Various Condensation Conditions. *J Therm Sci 2019 28:4*, vol. 28, no. 4, pp. 621–634, Jul. 2019, doi: 10.1007/S11630-019-1069-9.

[15] Lei B, et al. Experimental study and theoretical analysis of a Roto-Jet pump in small scale organic Rankine cycles. Energy Convers Manag Mar. 2016;111:198–204. https://doi.org/10.1016/j.enconman.2015.12.062.

[16] Feng Y Qiang, et al. Experimental investigation of a R245fa-based organic Rankine cycle adapting two operation strategies: Stand alone and grid connect. Energy Dec. 2017;141:1239–53. https://doi.org/10.1016/J.ENERGY.2017.09.119.

[17] Xu W, Zhang J, Zhao L, Deng S, Zhang Y. Novel experimental research on the compression process in organic Rankine cycle (ORC). Energy Convers Manag Apr. 2017;137:1–11. https://doi.org/10.1016/J.ENCONMAN.2017.01.025.

[18] Yang Y, Zhang H, Xu Y, Zhao R, Hou X, Liu Y. Experimental study and performance analysis of a hydraulic diaphragm metering pump used in organic Rankine cycle system. Appl Therm Eng Mar. 2018;132:605–12. https://doi.org/10.1016/J.APPLTHERMALENG.2018.01.001.

[19] Yang Y, Zhang H, Xu Y, Yang F, Wu Y, Lei B. Matching and operating characteristics of working fluid pumps with organic Rankine cycle system. Appl Therm Eng Sep. 2018;142:622–31. https://doi.org/10.1016/j.applthermaleng.2018.07.039.

[20] D'Amico F, et al. Semi-empirical model of a multi-diaphragm pump in an Organic Rankine Cycle (ORC) experimental unit. Energy Jan. 2018;143:1056–71. https://doi.org/10.1016/j.energy.2017.10.127.

[21] Zakeralhoseini S, Schiffmann J. Analysis and modeling of the tip leakage flow on the performance of small-scale turbopumps for ORC applications. Appl Therm Eng 2022:119160. https://doi.org/10.1016/j.applthermaleng.2022.119160.

[22] Zakeralhoseini S, Schiffmann JA. The effects of the tip clearance on the performance of small-scale turbopumps for ORC applications; analysis and

modelling. In: *Proceedings of the 6th International Seminar on ORC Power Systems*, 2021, vol. 2021, no. 112. [Online]. Available: http://infoscience.epfl.ch/record/289985.

[23] Gülich J. Centrifugal pumps. Berlin, Heidelberg: Springer; 2010. Accessed: Jul. 01, 2019. [Online]. Available:.

[24] Zakeralhoseini S, Schiffmann J. The influence of splitter blades and meridional profiles on the performance of small-scale turbopumps for ORC applications; analysis, neural network modeling and optimization. Therm Sci Eng Prog 2023;39: 101734. https://doi.org/10.1016/j.tsep.2023.101734.

[25] Nourbakhsh A, Jaumotte A, Hirsch C, Parizi HB. Turbopumps and pumping systems. Springer Science & Business Media; 2007.

[26] Japikse D, Marscher W, Furst R. Centrifugal pump design and performance. White River Junction, Vermont: Concepts NREC; 2006.

[27] Schulz H. "Kreiselpumpen," in *Die Pumpen*, Springer, 1967, pp. 7–233.

[28] Stepanoff AJ. Radial-und Axialpumpen. Springer; 1959.

[29] Nourbakhsh SA. Turbomachinery. Tehran: University of Tehran Press; 2005.

[30] Lobanoff VS, Ross RR. Centrifugal pumps: design and application. Elsevier; 2013.

[31] Menter F, Kuntz M, Langtry RB. Ten years of industrial experience with the SST turbulence model. Heat Mass Transf 2003;4.

[32] Versteeg HK, Malalasekera W, *An introduction to computational fluid dynamics: the finite volume method*. Pearson education, 2007.

[33] Rhie CM, Chow W-L. Numerical study of the turbulent flow past an airfoil with trailing edge separation. AIAA J 1983;21(11):1525–32.

[34] "ANSYS CFX-Pre User's Guide." Mar. 2021.

[35] MATLAB, *version 9.12.0 (R2022a)*. Natick, Massachusetts: The MathWorks Inc., 2022.

[36] Lemmon EW, Bell IH, Huber ML, McLinden MO. NIST Standard Reference Database 23: Reference Fluid Thermodynamic and Transport Properties-REFPROP, Version 10.0, National Institute of Standards and Technology. Gaithersburg: Standard Reference Data Program; 2018.

[37] Moffat RJ. Describing the uncertainties in experimental results. Exp Therm Fluid Sci 1988;1(1):3–17. https://doi.org/10.1016/0894-1777(88)90043-X.

[38] K. Rosset O. Pajot J. Schiffmann Experimental Investigation of a Small-Scale Organic Rankine Cycle Turbo-Generator Supported on Gas-Lubricated Bearings J Eng Gas Turbine Power 143 5 2021 pp. 1–14,51015 10.1115/1.4049988.

[39] Rosset K. "Small-scale organic Rankine cycle turbo-generator for waste heat recovery on truck engine," p. 186, 2020, doi: 10.5075/epfl-thesis-10347.